Rijksuniversiteit Groningen

Bachelor Thesis

Surface Flatness Inspection by Shack-Hartman Wavefront Sensing

Abstract

High resolution Fabry-Perot performance is a requirement for future mission concepts, including Origin's far-infrared observations to resolve narrow spectral bands of water and deuterium, important for the study of water transport in protoplanetary disks. Zero-gravity sagging and thermo-elastic processes can cause deviations in the flatness of its wafers, decreasing the angular resolution of the etalon. A concept for a flatness inspection tool for wafers is suggested with the use of Shack-Hartmann wavefront sensing. This method has the advantage of robustness to wavefront vibrations and internal alignment errors. A functional broadboard is built, automated and tested with a wafer of d=40mm. The wafer is subsequently compared with an interferometer measurement for cross-calibration. The total RMS surface error of the wafer was found to be $5.31 \pm 1.37 \mu m$ and $6.50 \pm 0.65 \mu m$ for the interferometer and Shack-Hartmann inspction tool respectively, mainly due to spherical deformation on the wafer. For future study it is suggested to test the breadboard to higher spatial-frequency surface errors and inspect stitching methods for a more extensive analyses.

Author:
R. Kuipers

Supervisors:
dr. ir. W. Jellema
R. Huisman

Contents

1 Introduction **3**
1.1 Scientific background . . . 3
1.2 Research objectives . . . 3

2 Theoretical Framework **6**
2.1 Shack-Hartmann Wavefront Sensing . . . 6
2.2 Zernike Polynomials . . . 7
2.3 Singular Value Decomposition . . . 9
2.4 Wavefront error analysis . . . 11

3 Experimental Setup **14**
3.1 Breadboard design . . . 14
3.2 Alignment procedure . . . 15
3.3 Controllers and Software . . . 16

4 Data acquisition **18**
4.1 Interferometer . . . 19
4.2 Shack-Hartmann . . . 19
4.3 Comparison . . . 21

5 Discussion **23**
5.1 Analysis of wavefront . . . 23
5.2 Sensitivity of setup . . . 24
5.3 Relative error . . . 25
5.4 Stitching . . . 25

6 Conclusion **27**

1 Introduction

1.1 Scientific background

After the launch of the Hubble Space Telescope (HST) in 1990 and the James-Webb Space Telescope (JWST) in 2021, a potential candidate for NASA's next large strategic science mission is the Origins Space Telescope (OST) (Meixner et al. (2019)). The motivation for the OST concept comes from previous scientific missions that observed in the optical range using the HST and the (near) infrared range using the JWST. OST intends to follow this trend of observing further into the far-infrared range. Whereas the Herschel Space Observatory (ESA mission, operational between 2009 and 2013) also observed in the far-infrared, OST will include a larger gain in sensitivity and improvement to the angular resolution by at least 4 orders of magnitude (Meixner et al. (2019)) through a larger and cooler telescope. Specific scientific topics OST aims to address with these improvements include the cosmic dawn and reionization, evolution of galaxies and black holes, protoplanetary disks, planet formation and the study of exoplanets (Meixner et al. (2019)).

An emerging scientific topic of interest is the study of water transport in protoplanetary disks (PPD). In colder outer regions of the PPD water freezes on the grains, and cores of potentially habitable planets might form (van Dishoeck et al. (2014)). Key diagnostic lines such as water and deuterium can be richly observed through narrow spectral lines in the far-infrared. High-resolution spectroscopy allows for measurements in line intensity and also allows for velocity distributions of these gases relative to the observer (Meixner et al. (2019)). The Planetary Origins and Evolution Multispectral Monochromator (POEMM) is a balloon-born project proposal by NASA Goddard Space Flight Center (2020) (in which SRON is a co-investigator) to investigate part of this science case, as a precursor towards OST.

A limiting factor is that H_20 and HD line intensities are relatively strong to the continuum of the PPD, but many such systems are weak in overall flux. Measuring such signals requires high resolving power instrumentation with high sensitivity (Meixner et al. (2019)). This can be achieved by cooling the telescope: The mission concept study report requires a cryocooler to keep the detector and telescope optics cooled at 50mK and 4K respectively (Meixner et al. (2019)). Other ways to improve sensitivity is through direct detection and dispersive optics such as a high-resolution Fabry-Perot etalon (Meixner et al. (2019)).

A limiting factor of the high-resolution Fabry-Perot performance is the quality of the mirror. Figure 1a illustrates an incident light beam reaching an ideal etalon cavity, such that a narrow spectral band is transmitted at $\lambda = 2d$, where d is the thickness of the cavity. In comparison with 1b, non-ideal wafers cause refraction from surface deviations and scattering from roughness on the surface. Refraction increases the FWHM of the spectral lines and causes noise from light scattering, decreasing the angular resolution of the etalon (Bartek et al. (2000)). Deviations from ideal flatness in mirrors can occur due to zero-gravity sagging and thermo-elastic stresses, significantly impacting the sensitivity of etalon wafers. For this reason surface errors of those wafers must be measured in detail.

1.2 Research objectives

This project introduces and explores a method for inspecting the surface flatness of such wafers with the use of Shack-Hartmann wavefront sensors (SHWS). SHWS are slope wavefront sensors, widely used within the field of adaptive optics (AO). In astronomy SHWS systems are recognised

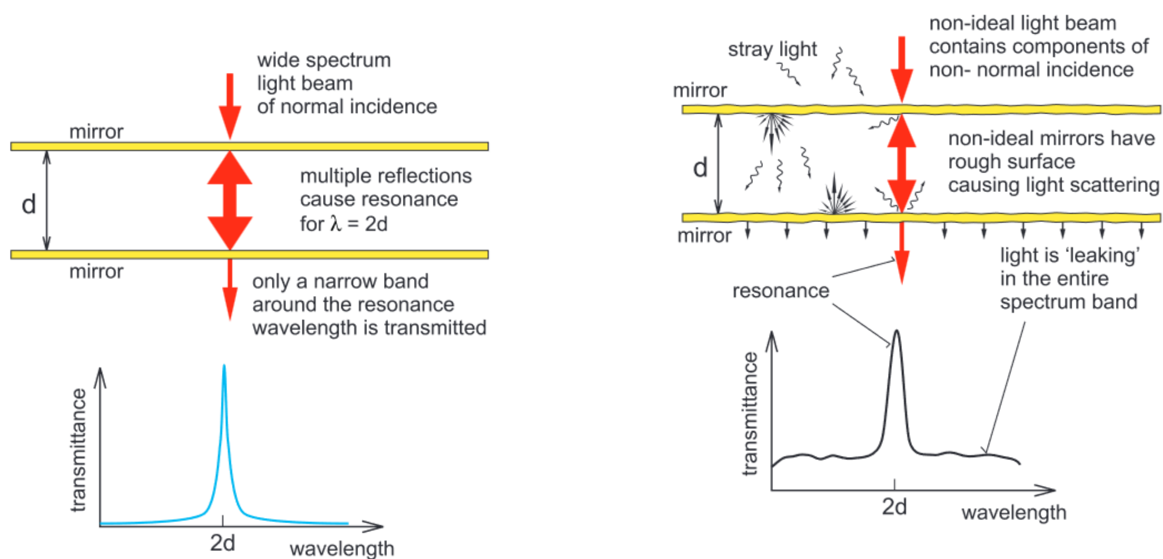

(a) An ideal setup of an optical resonator produce clear spectral lines.

(b) In reality mirrors are not ideal and cause refraction and scattering, decreasing the sensitivity of the optical resonator.

Figure 1: Comparison between ideal and non-ideal behaviour of Fabry-Perot optical resonators (Bartek et al. (2000)).

as methods for measuring wavefront distortions caused by atmospheric disturbances, to provide aberration corrections to ground-based telescope images (either with the use of bright reference stars or artificially reflective lasers, Hardy (1998)). Although this paper will inspect the use of SHWS to improve the performance of astronomical instruments, it will look at improving the performance of the instruments themselves. The materials this project will investigate are High-resolution Fabry-Perot silicon wafers. These silicon wafers are high quality, lossless far-infrared materials suitable for high-infrared spectroscopy.

The idea of the project is to construct an optical breadboard which provides a proof of principle of a SHWS inspection tool. A collimated light beam will shine on 40-50mm wafers and their reflected wavefronts will be directed to the Shack-Hartmann for a surface analysis of the wafer. The breadboard will include 6x and 12x magnifications of the beams using off-axis parablic mirrors for covering a more extensive analysis of the wafer. Two linear stages will be provided which can be controlled both manually and automatically, to allow a full surface flatness analysis of the wafer through a chosen stitching technique.

The following questions are of interest for the functionality of the inspection tool:

- Can a functional demonstration of the measurement of surfaces flatness by the proposed method be provided?
- Assuming functional demonstration, how well and how accurate can surface errors and deviations be measured?
- How well can smaller maps be stitched to larger composite maps while maintaining its resolution?

A theoretical framework of the SHWS inspection tool, as well as the error handling of wavefronts will be provided in this thesis. The proposed setup is aligned, tested and compared with an interferometer measurement. The functionality and sensitivity of the setup is discussed. Finally, suggestions for future steps are taken to provide a complete analysis for inspecting the surface flatness of a wafer.

2 Theoretical Framework

2.1 Shack-Hartmann Wavefront Sensing

A Shack - Hartmann Wavefront Sensor is a tool used in various fields of adaptive optics to inspect surface deviations. The instrument has a microlens array which divides an incoming beam into smaller separate beams and refracts them towards a sensor. Upon an uniformly planar wavefront incident to the microlens (Define beams travelling in the z direction), the beams will refract to a regularly spaced grid on the sensor (Set reference x = y = 0 of each grid) as can be shown on fig.2. Upon distortions in the wavefront, the beams will deviate by $x = \delta x$ and $y = \delta y$ (Neal et al. (2002)). This lateral displacement is proportional to the local wavefront error slope. By measuring an array of slopes the wavefront error can be reconstructed by integrating the gradients.

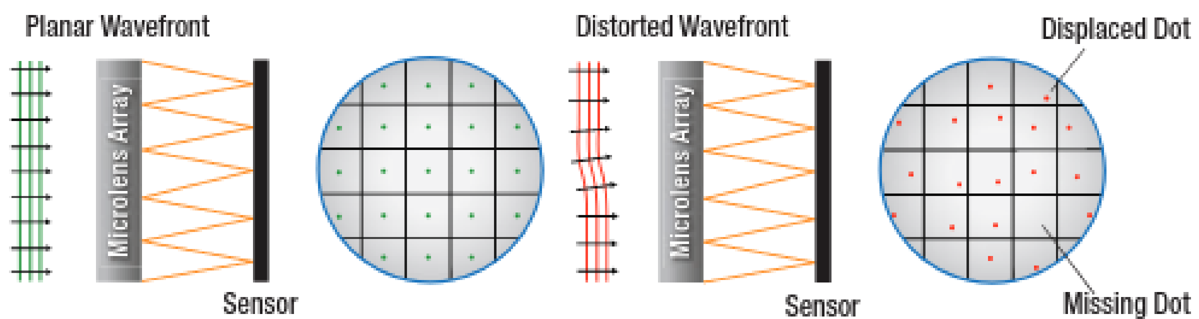

Figure 2: Comparison of a planar and distorted wavefront interacting with the wavefront sensor. Distorted wavefronts will deviate from the focal spot of the grid, if the deviation reaches away from a grid it will not receive data Thorlabs (2022).

Two properties which can be derived is the Sensitivity θ_{min} and the Dynamic Range θ_{max}. Both are determined respectively by (Thorlabs (2022)):

$$\theta_{min/max} = \frac{r_{min/max}}{f_{ML}}, \quad \text{(Slope)} \tag{1}$$

where $r_{min} = \sqrt{x_{min}^2 + y_{min}^2}$ is the minimum measureable offset from the reference grid which depends on the pixel size, algorithm and signal to noise ratio of the sensor. $r_{max} = \frac{d}{2}$ is the maximum measureable displacement, which depends on the diameter d of the microlens. f_{ML} is the focal length of the microlens.

Equation (1) tells us intuitively the dynamic range of a measurement can be extended either by decreasing the focal length of the sensor, or alternatively compressing the information of the incoming beam to fit the diameter of the microlens. This also increases r_{min}, meaning a decrease in sensitivity of the signal. Alternatively, decreasing the dynamic range could result in a loss of data, when the measured displacement r exceeds r_{max}. The focal length of the system must thus be considered based on the dynamic range and sensitivity requirement of the inspection.

2.2 Zernike Polynomials

To quantify the observed wavefronts analytically, a solution can be given in terms of Zernike polynomials. The polynomials were developed by Fritz Zernike (1933) to approach a problem in optimizing optical instruments with deviations comparable to its incoming wavelengths, applying wave diffraction theory rather than an analytical treatment of the mirrors. The result became an infinite sequence of polynomials that can represent wavefront deviations of a chosen order.

The power of Zernike polynomials lies in that they are both orthogonal and continuous in nature within a unit disk. The orthogonality conditions allows any wavefront to be represented as a set of Zernike polynomials on a unit circle, as the inner products of orthogonal functions are always zero by definition. Continuity of these polynomials are a mandatory condition to ensure orthogonality on a unit circle.

For an integer $n \geq 0$ and integers $n - |m| \geq 0$, Zernike polynomials are defined (Lakshminarayana and Flek (2011)):

$$Z_n^m(\rho, \theta) = N_n^m \begin{cases} R_n^{|m|}(\rho) cos(m\theta) & \text{if } m \geq 0 \\ R_n^{|m|}(\rho) sin(|m|\theta) & \text{if } m < 0 \end{cases},$$

where the radial part R is given by:

$$R_n^{|m|}(\rho) = \sum_{k=0}^{\frac{n-|m|}{2}} \frac{(-1)^k (n-k)!}{k!(\frac{n+m}{2}-k)!(\frac{n-m}{2}-k)!} \rho^{n-2k}, \tag{2}$$

and the normalisation coefficient N is given by:

$$N_n^m = \sqrt{\frac{2n+2}{1+\delta_{m0}}}, \tag{3}$$

Zernike polynomial Table					
Z_n^m	Index (i)	n	m	Z_i	Name
Z_0^0	0	0	0	1	Piston
Z_{-1}^1	1	1	-1	$2\rho \sin\theta$	Tip
Z_1^1	2	1	+1	$2\rho \cos\theta$	Tilt
Z_{-2}^2	3	2	-2	$\sqrt{6}\rho^2 \sin 2\theta$	Oblique Astigmatism
Z_0^2	4	2	0	$\sqrt{3}(2\rho^2 - 1)$	Defocus
Z_2^2	5	2	+2	$\sqrt{6}\rho^2 \cos 2\theta$	Vertical Astigmatism
Z_{-3}^3	6	3	-3	$\sqrt{8}\rho^3 \sin 3\theta$	Vertical trefoil
Z_{-1}^3	7	3	-1	$\sqrt{8}(3\rho^3 - 2\rho)\sin\theta$	vertical coma
Z_1^3	8	3	+1	$\sqrt{8}(3\rho^3 - 2\rho)\cos\theta$	Horizontal coma
Z_3^3	9	3	+3	$\sqrt{8}\rho^3 \cos 3\theta$	Oblique trefoil

Table 1: A table of the first 10 Zernike indexes and their respective names.

Table 1 above shows the first 10 Zernike polynomial functions, as well as their referred names. Figure 3 shows a figure made in Python of the first 10 polynomial functions (excluding piston, which is just a constant). It should be noted in Fig. 3 that there are no axes for the unit circles, this will be the case for all Zernike polynomials. The reason is the that the polynomials are defined in a unit circle, the radius of the polynomial is always one unit. The units can be defined in the experiment.

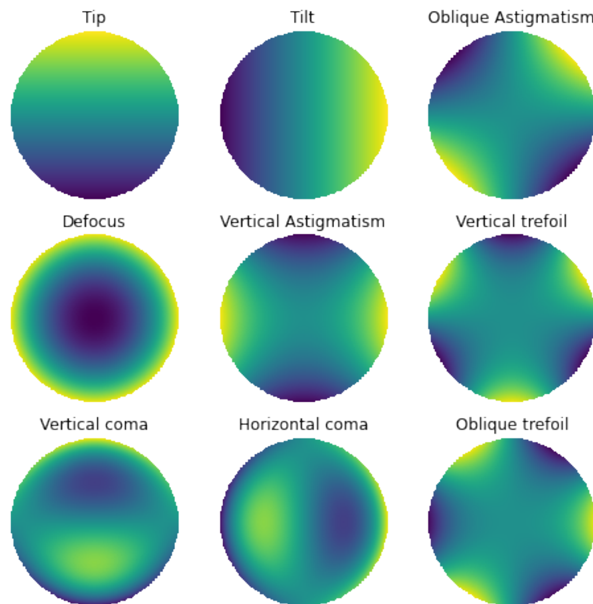

Figure 3: A visual representation of the first 10 Zernike polynomials (excluding piston). They are ordered in rows from right to left, top to bottom. It can be seen for example that 4th index Zernike polynomial located at the middle right is indeed the focus. Made in Python.

It is evident from Fig. 3 that each Zernike polynomial provide information of a specific deviation, and the order n provides an order to the deviation. A polynomial of order n = 0 is called the piston, a constant that represents the mean value of the wavefront. A polynomial of order n = 1 provides a radially linear function, informatively it represents the tilt (mode m = -1 is vertical, m = 1 horizontal) of the wavefront. Polynomials of order n = 2 represent astigmatism and defocus on the wavefront dependent on your chosen mode. Polynomials of order n = 3 represent third order deviations such as trefoil (astigmatism with 3 peaks/valleys) and coma. Higher orders continue this pattern and show any deviations that behave in that order.

As Zernike polynomials are orthogonal, they form a complete set and so the wavefront $W(\rho, \theta)$ can be defined as a combination of linearly independent Zernike polynomials (Lakshminarayana and Flek (2011)):

$$W(\rho, \theta) = \sum_{m,n} C_n^m Z_n^m(\rho, \theta) = \langle Z|c \rangle, \tag{4}$$

The implication is that given a set of Zernike polynomials with their respective amplitudes, you can produce a wavefront with deviations provided in terms of Zernike polynomials. Figure 4 represents a test wavefront, combining the first 3 orders of polynomials with a random set of normally distributed coefficients.

The ability to create a wavefront is limited by the number of Zernike polynomials used. Wavefronts with higher order deviations are difficult to create if the number of Zernike polynomials used to create the wavefront is at a lower order. Increasing the number of Zernike polynomials allows more information to be stored in the wavefront, however singular value decomposition (see section 2.3) will show that the number of Zernike polynomials useful for wavefront reconstruction is also limited by the number of degrees of freedom of the setup.

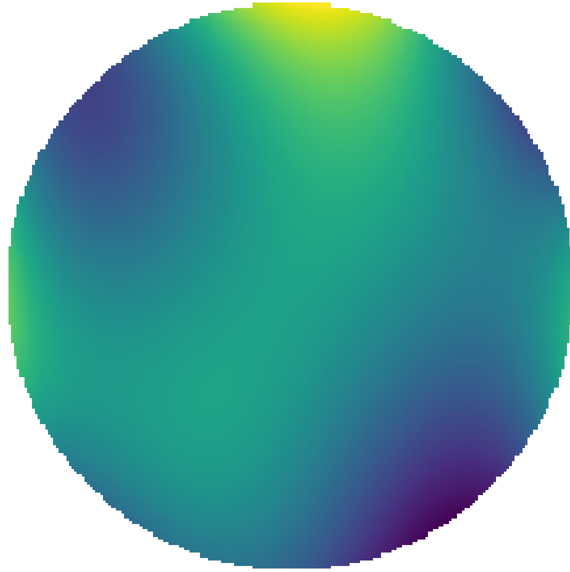

Figure 4: A 188x188 pixel wavefront image created by summing the first 10 Zernike polynomials (excluding piston) with a random set of normally distribution of coefficients. Created with Python.

2.3 Singular Value Decomposition

Just as wavefronts can be constructed by applying coefficients to Zernike polynomials, coefficients can be extracted from wavefronts in terms of Zernike polynomials. Representing the wavefront as an N × N matrix W (N is the length of the image in pixels), C is a 1 × M matrix and Z is a M × N × N matrix (M is the number of Zernike polynomials used), linear algebra tells us that:

$$\begin{aligned} W &= Z \cdot C, \\ Z^{-1}W &= Z^{-1}(Z \cdot C), \\ &= (Z^{-1}Z) \cdot C, \\ &= I \cdot C, \\ Z^{-1}W &= C. \end{aligned} \tag{5}$$

It turns out that the Zernike polynomial matrix Z is often not invertible. The alternative to the inverted matrix is the pseudo-inverse, obtained through singular value decomposition, which gives a least-squares approximation to (5):

$$
\begin{aligned}
Z &= U\Sigma V^T \\
Z^{-1} &= V\Sigma^{-1}U^T \\
Z^{-1}Z &= V\Sigma^{-1}U^T U\Sigma V^T = V\Sigma^{-1}\Sigma V^T = VV^T = I.
\end{aligned} \tag{6}
$$

Thus by decomposing Z into unitary and diagonal matrices and subsequently inverting U, Σ and V^T, you can find the pseudo-inverse of Z, this procedure is called Singular Value Decomposition (SVD). For a 2-dimensional M $\times$ N matrix Z like in equation 6, U represents a unitary N $\times$ N matrix, Σ represents the rectangular diagonal M $\times$ N matrix, and V^T represents a unitary M $\times$ M matrix. Although the Z matrix is 3-dimensional, it can be solved by turning it into a 2-dimensional matrix by reshaping the N $\times$ N Zernike polynomials into a N^2 coloumn vector. Figure 5 shows the result of a reconstructed wavefront from coefficients found using we wavefront in fig.4 and the SVD method. The difference between the two sets of coefficients are numerically negligible and the wavefronts appear identical.

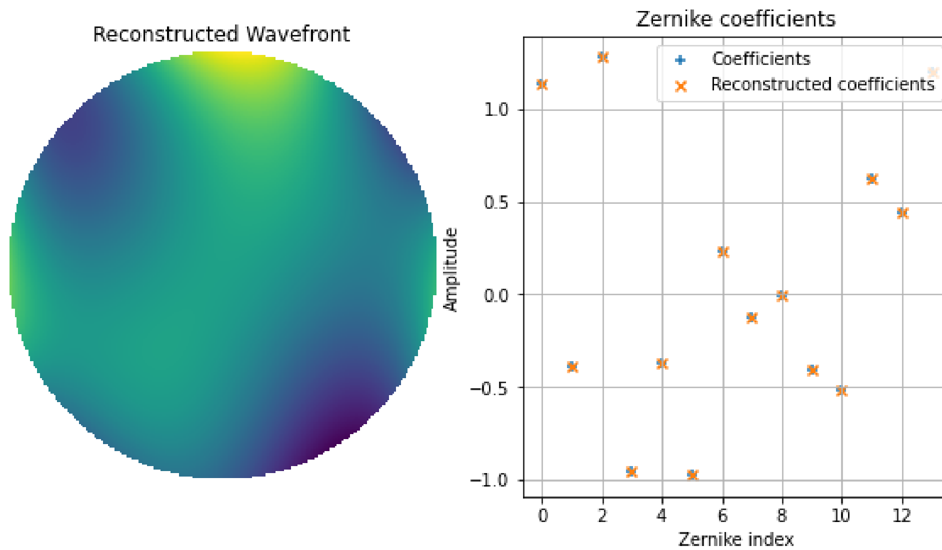

Figure 5: Given a wavefront with an unknown set of coefficients, the coefficients were found using SVD and the wavefront is reconstructed. The difference between the initial and reconstructed set of coefficients at numerical accuracy ($\sim 10^{-16}$). Created with Python.

The useful information lies in the Σ values of the wavefront matrix Z, these are the coefficients that inverted with the wavefront matrix returns the coefficient matrix. The inverted matrix was calculated by inverting all diagonal coefficients in the matrix. Should the initial coefficient equal less than 0.01, a condition changes this value to 0.01 to ensure the inverted coefficient does not blow up. This occasionally occurs because the number of coefficients on your Σ matrix is limited on the rank of Z. When a new coloumn is a linear combination of one of the other coloumns, the coefficient of this coloumn becomes 0. The rank is dependent on the degrees of freedom available to the system that creates the wavefront, and provides a limit to the usefulness of increasing the number of Zernike polynomials to resolve your wavefront.

2.4 Wavefront error analysis

Given a uniformly planar and incident wavefront, all Zernike polynomials of first and higher order will be 0. If we insert a uniformly planar wavefront into an imperfect optical system and measure the returning wavefront, we can call this matrix the wavefront error (WFE). The WFE that can be defined in (4) in polar coordinates can be transformed to cartesian coordinates:

$$WFE(x_i, y_i) = \sum_{m,n} C_n^m Z_n^m(x_i, y_i). \tag{7}$$

One of the many strengths of finding a WFE in this way is that given a normalized and summed set of Zernike polynomials (with their respective coefficients), deviations from the ideally flat slope of the wavefront represents the RMS error Sacek (2006). By removing the piston, tip and tilt of the wavefront (with other words removing 0 and 1st-order terms), your resulting WFE produces an image of N $\times$ N pixels of an ideally incident wavefront, where the RMS of each pixel equals the absolute wavefront error of that pixel:

$$RMS_{WFE(x_i,y_i)} = \sqrt{\frac{\Sigma_{j=1}^{N}\Sigma_{k=1}^{N}(WFE(x_i,y_i))^2}{N_j N_k}}. \tag{8}$$

For finding the total RMS of the system, it is worth remembering that the wavefront represents a linear combination of Zernike polynomials, the strengths of which are given by their coefficients. Since the length of each Zernike polynomial is $\rho = 1$ within its unit disk they sum to become one unit, the coefficient provides the amplitude of this unit. This has been tested in the code, although the computation is discrete the RMS of a Zernike polynomial is practically 1. The RMS of a wavefront from a certain Zernike index is the absolute value of its coefficient Sacek (2006):

$$RMS_{WFE_{Z_i}} = \sqrt{\frac{\Sigma_{j=1}^{N}\Sigma_{k=1}^{N}(WFE_{Z_i})^2}{N_i N_j}} = \sqrt{\frac{\Sigma_{j=1}^{N}\Sigma_{k=1}^{N}(C_i Z_i)^2}{N_i N_j}} = \sqrt{\frac{\Sigma_{j=1}^{N}\Sigma_{k=1}^{N}C_i^2}{N_i N_j}} = \sqrt{C_i^2} = |C_i|. \tag{9}$$

The total RMS of the wavefront error of two or more (Z) Zernike polynomials is the square root of the sum of the coefficients squared Sacek (2006):

$$\begin{aligned}
RMS_{WFE} &= \sqrt{\frac{\Sigma_{j=1}^{N}\Sigma_{k=1}^{N}(WFE)^2}{N_j N_k}}, \\
&= \sqrt{\frac{\Sigma_{j=1}^{N}\Sigma_{k=1}^{N}(\Sigma_{n,m}C_m^n Z_m^n)^2}{N_j N_k}}, \\
&= \sqrt{\frac{\Sigma_{j=1}^{N}\Sigma_{k=1}^{N}(C_1^2 Z_1^2 + C_2^2 Z_2^2 + ... + C_Z^2 Z_Z^2 + \text{cross terms})}{N_j N_k}}, \\
&= \sqrt{\frac{\Sigma_{j=1}^{N}\Sigma_{k=1}^{N}(C_1^2 Z_1^2)}{N_j N_k} + \frac{\Sigma_{j=1}^{N}\Sigma_{k=1}^{N}(C_2^2 Z_2^2)}{N_j N_k} + ... + \frac{\Sigma_{j=1}^{N}\Sigma_{k=1}^{N}(C_Z^2 Z_Z^2)}{N_j N_k}}, \\
&= \sqrt{RMS_{WFE_{Z_1}}^2 + RMS_{WFE_{Z_2}}^2 + ... + RMS_{WFE_{Z_Z}}^2}, \\
&= \sqrt{\Sigma_i^Z C_i^2}.
\end{aligned} \tag{10}$$

Equation (10) is possible due to the orthogonality of the polynomials, all cross terms average out to 0.

To find the Zernike coefficients of a WFE, which can be found from a measured wavefront M, subtracted by a reference wavefront R, the orthogonal nature of Zernike polynomials again allow us find the coefficients directly (formulated in matrix notation):

$$WFE = M - R = ZC_M - ZC_R = Z(C_M - C_R) = ZC_{WFE} \implies C_{WFE} = C_M - C_R \tag{11}$$

To find the RMS of this WFE from measuring M and R:

$$\begin{aligned}
RMS_{WFE} &= \sqrt{\frac{\Sigma_{j=1}^{N}\Sigma_{k=1}^{N}(WFE)^2}{N_j N_k}}, \\
&= \sqrt{\frac{\Sigma_{j=1}^{N}\Sigma_{k=1}^{N}(M-R)^2}{N_j N_k}}, \\
&= \sqrt{\frac{\Sigma_{j=1}^{N}\Sigma_{k=1}^{N}(ZC_M - ZC_R)^2}{N_j N_k}}, \\
&= \sqrt{\frac{\Sigma_{j=1}^{N}\Sigma_{k=1}^{N}(Z(C_M - C_R))^2}{N_j N_k}}, \\
&= \sqrt{\frac{\Sigma_{j=1}^{N}\Sigma_{k=1}^{N}(ZC_{WFE})^2}{N_j N_k}}, \\
&= \sqrt{\Sigma_i^Z C_{WFE,i}^2}.
\end{aligned} \tag{12}$$

These solutions are very simple to compute and allow us to make an error analysis of the wavefront. To demonstrate that the total RMS of a wavefront error is in fact not dependent

on the signs of the coefficients, a demonstration of this phenomena is shown on on Fig.6. By defining the matrices $WFE_{1,2} = Z_{10} \pm 2Z_{14}$ and by taking the square root of the sum of all elements of their matrices squared, you receive the same wavefront errors of both matrices. The total RMS of a wavefront is simply dependent the magnitude of the Zernike coefficients: $RMS = \sqrt{1^2 + (\pm 2)^2} = 2.23$.

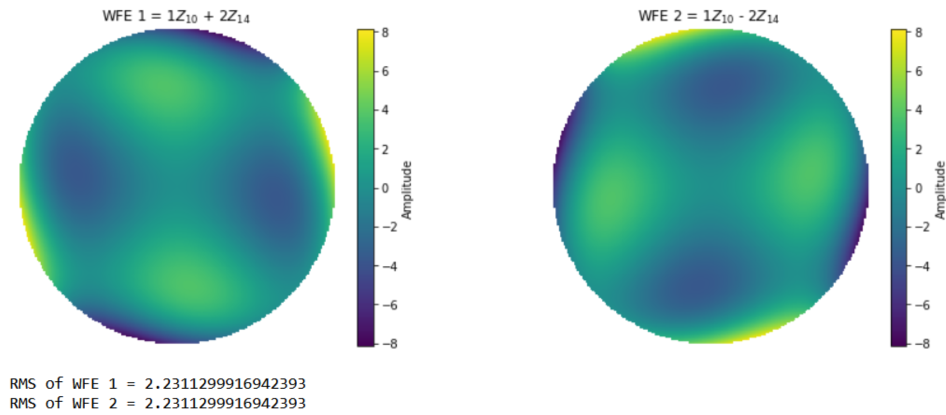

Figure 6: Demonstration of two different wavefronts whose 14th Zernike index have opposite signs, yet their magnitudes still yields the same RMS for their wavefront error. Created with Python.

3 Experimental Setup

3.1 Breadboard design

The breadboard consists of the following components:

- A laser diode source operating at 2V to up to 50mA with wavelength $\lambda = 633\ nm$,
- Wavefront sensor, type WFS300-14AR (Thorlabs)
- 4 off-axis parabolic mirrors (M1-M4, also from Thorlabs):
  - M1 and M3 have a diameter of 1 inch (25.4 mm) and a reflected focal length (RFL) of 2 inches (50.8 mm)
  - M2 has a diameter of 1 inch (25.4 mm) and a RFL of 4 inches (101.6 mm)
  - M4 has a diameter of 3 inches (25.4 mm) and a RFL of 6 inches (152.4 mm)
- 2 beamsplitters (BS1, BS2)
- Supporting adjustable mounts
- Supporting linear stages
- A reference mirror, 10 cm
- A sample wafer

All mirrors have a reflected wavefront error of $< \lambda/4$. All mirrors have mounts which can rotate the mirror with arcminute precision and linear stages in three orthogonal directions which can translate the mirrors with micrometer precision. The beamsplitters are oversized to avoid vignetting of the laserbeam.

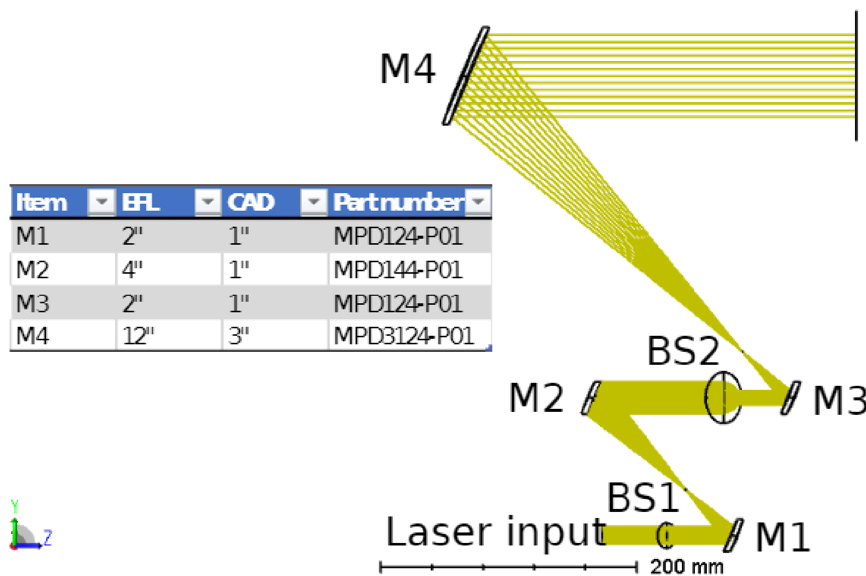

Item	EFL	CAD	Partnumber
M1	2"	1"	MPD124-P01
M2	4"	1"	MPD144-P01
M3	2"	1"	MPD124-P01
M4	12"	3"	MPD3124-P01

Figure 7: Zemax diagram of setup. The part numbers are the Thorlabs mirror names.

The design has three functionalities in mind. The first is a reference mirror which can be placed behind the sample wafer. The reference mirror will be placed incident to the incoming wavefronts for complete reflection which includes internal alignment errors, surface errors and the SH sensor error. A measurement with the reference mirror is to calculate the wavefront distortion of the setup, this will be the reference measurement. Subsequently a test sample can be placed in front of the reference mirror and another measurement will be made. Since the only difference between the two measurements are the replacement of the sample mirror and reference mirror, the difference in observed Zernike coefficients must be because of the contribution of the sample mirror. The orthogonality of Zernike polynomials allows us to determine the Zernike coefficients of the sample mirror, and subsequently reconstruct the image:

$$C_{sample} = C_{raw} - C_{ref} \tag{13}$$

The second set of functionalities are beam magnifications, this will be constructed using beam expanders. A pair of off-axis parabolic mirrors are aligned at their RFL for a common focus. The beam expansion is equal to the ratio of their focus:

$$\text{Beam expansion} = \frac{f_2}{f_1}, \tag{14}$$

As shown by the reflective focal lengths on Fig. 7, there are beam expansions of factor 2 between the mirrors M1 and M2, as well as a factor 6 for M3 and M4. The mirrors are off-axis by 45 degrees to maintain the compact design in Fig. 7. There is vignetting between M1 and M2 due to M2 having twice the reflected focal length, however the same diameter as M1. This vignetting is acceptable, the signal that is reflected will still be sufficiently strong. M4 should fully capture the signal coming from M3 and vica versa. Beam splitter placed between M1 and M2, as well as M3 and M4, allows the SHWS to receive a reflected beam of magnification 12x or 6x respectively. The choice of magnification depends on the desired sensitivity and dynamic range requirement for the Shack-Hartmann sensor.

The last functionality is automation of two linear stages which can move the sample mirror in XY-directions. With this functionality different parts of the mirror can be analysed and stitching techniques may be used for a full flatness analysis of the mirror.

3.2 Alignment procedure

For the exact alignment of all components of the setup an industrial theolodite with arcsecond precision was used. A light source is emitted from the theolodite to a mirror, this mirror is aligned when the observer can recover the light source through the theolodite's cross lens. It can be assumed that all mirrors are aligned to at least arcminute precision using this method. All components can fit within a movable thorlabs table.

A demonstration of aligning M1 is shown on Fig. 8. Two flat mirrors are used for referencing, let the larger mirror be called FM1 and the other FM2. FM1 is placed and aligned and set at 0 degrees to set the axes. The theolodite is then rotated 135 degrees, where FM2 is aligned. Returning the theolodite to 0 degrees using our reference frame BM1, M1 can be placed in front of BM1 and aligned (both in rotation and translation). The M1 can reflect a light sources 45 degrees, if aligned perfectly the light should reach and reflect from FM2, and back to the M1

Figure 8: Alignment of the M1 mirror, with the use of 2 reference mirrors.

which directs it to the theolodite. The alignment of the mirrors include using optical methods of this sort. A reflection on the final quality of the alignment of the setup will be discussed in section 5.2. An image of the final setup is shown on Fig. 9.

Figure 9: Finalised setup of Shack-Hartmann inspection tool.

3.3 Controllers and Software

The Thorlabs SHWS has its own graphical user interface to take measurements, both of the WFE of each microlens spot and the Zernike coefficients. The resolution of this SHWS is 1440 x 1080 pixels, which with grid lengths of 63 pixels produces 23x17 microlens spots (Thorlabs (2022)).

The Thorlabs laser diode operates actively at 20mA during the course of the experiments,

although 50mA is possible a signal could be measured at 10mA and it was not desired to overheat the diodes. The diode could be run manually from the controller, however this controller also has its own graphical user interface which can be run from your laptop. The supporting linear stages are from standa, which can be run manually from the controller or run using python code on Xilab. As of June 2022 an OS if Windows 10 or older is required, other the Python libraries will not be recognised.

4 Data acquisition

To test the functionality of the Shack-Hartmann Wavefront sensor, the wavefront error of the sample wafer will also be measured by an interferometer. The interferometer is used since the initial Zernike coefficients of the test samples were not known. Measuring the sample with two methods allows for a comparison study of the inspection tool.

Several tests were carried out earlier in the thesis to test the functionality of the setup. Their results will not be covered, but they prepared us for a more extensive and careful measurement and analysis of this experiment. For example, Zernike coefficients above the order $n = 5$ will not be measured, it will be demonstrated the wafer only has measurable coefficients up to n=2. A circular aperture will be made to mask the wafer, to a size both the interferometer and the Shack-Hartman can resolve for a fair comparison.

The interferometer included its own graphical user interface (IntelliWave) which had the functionality of calculating the Zernike terms of a wavefront and their respective RMS, by taking 5 measurements and providing a best fit. Previous measurements of the raw wavefront yielded practically identical Zernike coefficients with the SVD method as shown on Fig. 5 to that of the GUI's Zernike coefficients. This is the same case for the Shack-Hartman wavefront sensor. Therefore the coefficients of the GUI will be used throughout the report unless stated otherwise.

For this experiment the test wafer used is a FZ Silicone Wafer, (N-Ph) $>$ 5000 Ohm-cm. Its thickness is 618 μm and has a diameter of 100mm. The Shack-Hartmann Wavefront sensor is 11.34 $mm \times 7.13$ mm in diameter, so a cardboard with a circular mask of 4.0 ± 0.1 cm was made so a full aperture would be visibility to both the interferometer and the SHWS with 12x magnification.

Raw data of measurements (units: μm, accuracy: nanometers)					
Coefficient	Interf.	Int. RMS	SH - raw	SH - ref	SH - sample
Z_0	- 0.000	0.481	- 5.677	- 2.055	- 3.622
Z_1	- 2.795	0.680	4.579	1.216	3.363
Z_2	- 0.905	0.680	2.279	1.754	6.300
Z_3	- 1.712	0.060	- 6.000	0.147	0.141
Z_4	- 4.898	0.833	- 1.052	- 0.538	- 0.514
Z_5	1.093	0.060	- 0.123	- 0.218	0.095
Z_6	- 0.184	0.070	0.006	0.009	- 0.003
Z_7	0.044	0.070	- 0.001	- 0.008	- 0.002
Z_8	0.049	0.070	0.002	- 0.010	0.012
Z_9	0.118	0.025	0.009	- 0.001	0.008
Z_{10}	- 0.148	0.028	- 0.004	- 0.003	- 0.001
Z_{11}	- 0.015	0.028	0.002	0.008	- 0.006
Z_{12}	- 0.054	0.028	0.004	- 0.003	0.007
Z_{13}	0.031	0.028	- 0.012	0.003	- 0.015
Z_{14}	0.031	0.028	0.003	- 0.010	0.013

Table 2: Raw data of the measurements of the wafer, as downloaded from the Interferometer and the Shack-Hartmann wavefront sensor. The SH sample is the difference between SH-raw and SH-ref. Some data will still need to be normalised, magnified or corrected, this is covered in section 4.1 and 4.2.

4.1 Interferometer

Because the GUI provides the Zernike 'terms' and their respective RMS they need to be normalized to be represented as coefficients. The GUI measures in nanometers, they are converted to micrometers to be consistent with unit used in this thesis.

The wavefront measured is a reflected wavefront, meaning a wavefront initially travelling in a direction z is now measured in -z. The sign of even functions (when m $<$ 0, the polynomial is a sin function) changes and so must be corrected to receive the same result as that of the Shack-Hartmann.

Figure 10 shows a reconstruction of the wavefront and their coefficients, it was 'masked' in the GUI to cover only visible aperture of the wafer.

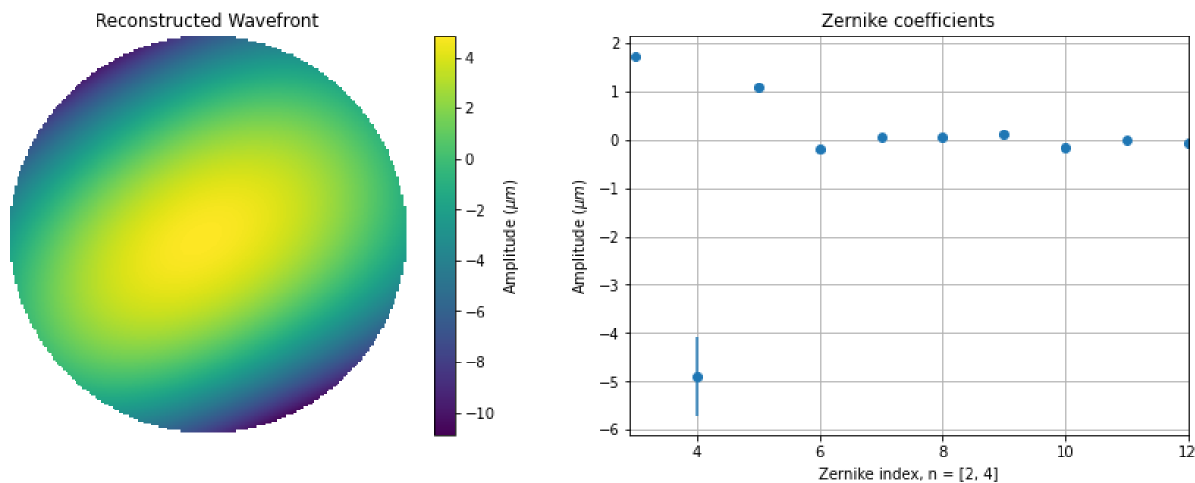

Figure 10: A wavefront is constructed and its (normalised) amplitudes and RMS graphed from the Zernike coefficients provided by the interferometer. See Table 2 for the raw data. Figure created with Python.

The RMS of each Zernike coefficient is provided by the GUI in nanometers. RMS units will be converted into micrometers for consistency. The total RMS of the wavefront is the sum of the Zernike coefficients (not including piston, tip, tilt):

$$RMS_{total} = \sqrt{\Sigma_{i=1}^{N} C_i^2} = 5.31 \pm 1.37 \mu m. \tag{15}$$

4.2 Shack-Hartmann

A raw measurement in this context constitutes a measurement with a reflection from a wafer instead of a reference mirror, the reference measurement constitutes the opposite. From these two measurements an image of the sample is created by subtracting the reference image from the raw image. The sensor does measure the entire wafer aperture of 4.0 ± 0.5 cm with 12x magnification. However a strong tip shown on Fig. 11 does not make the aperture visible in the images, it is reconstructed in Fig. 12 to show the shape of this wafer.

According to theory, subtracting the coefficients of the reference measurements from the raw measurement provides the coefficients of the wafer. The coefficients measured by the sensor must

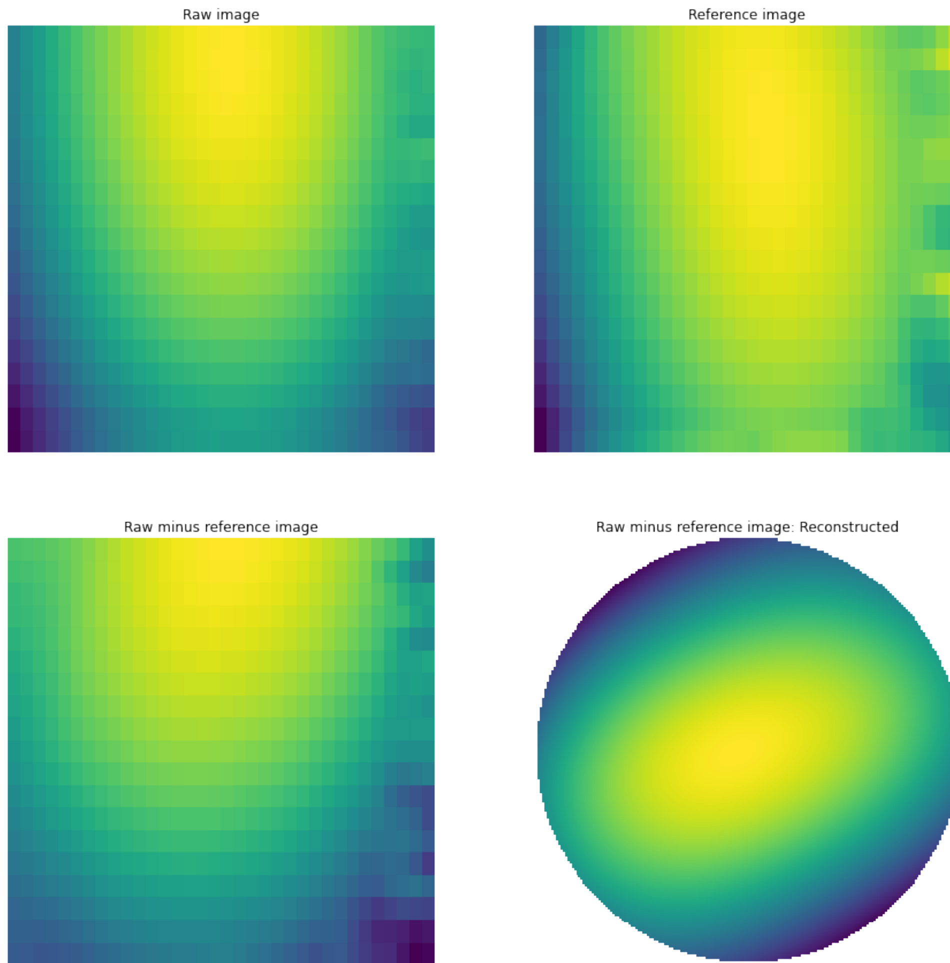

Figure 11: An image is taken of the wafer by subtracting the amplitudes of the reference image from the raw image. Significant tip blurs the image of the wavefront error, a reconstruction without tip and tilt are shown within a unit disk. created with Python.

be multiplied by a factor 12 as this was the chosen magnification of the setup. The process if magnifying the Zernike coefficients sounds contradictory at first as wave amplitudes are conserved during beam expansion and compression. It must be remembered that the sensor calculates the Zernike coefficients of a wavefront within its own unit disk, given by length r=d/2 of the of the polynomial. Upon a scaling of the unit disk the coefficients are still conserved within the disk, however the bounds of the disk are magnified which increases the total wavefront error and so also the total Zernike contributions to the wavefront. This is supported empirically where initial measurements at different scales also showed the Zernike coefficients to multiply with this scale.

Repeated initial measurements found the Zernike values to deviate by no more than $10nm$. Assuming this as the deviation of both the raw measurement and the reference measurement and magnifying the function with a factor 12, the uncertainty of the coefficients of the sample becomes $\sigma_{sample} = \sqrt{\sigma_{raw}^2 + \sigma_{ref}^2} = \sqrt{0.12^2 + 0.12^2} = 0.169\mu m$ by error propagation.

The Shack-Hartmann also reflects its wavefront at the wafer/reference mirror and so produces an inverted image, however this wavefront is again reflected by the beam splitter, inverting the

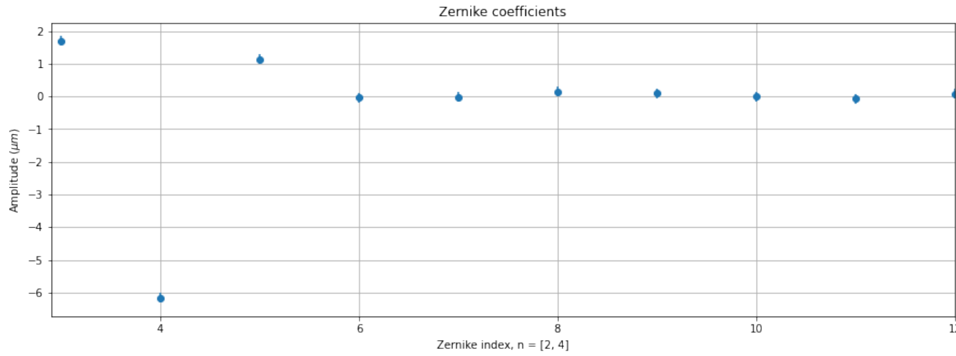

Figure 12: The reconstructed wavefront is graphed, from the Zernike coefficients provided by the Shack-Hartmann wavefront sensor. Created with Python.

image a second time. It can also be seen from Figure 7 that two off-axis parabolic mirrors also invert the image of a collimated beam, so for a x12 magnification image the wavefront is inverted four times. If the beam-splitter was placed at BS2 for a x6 magnitude the wavefront would be inverted an odd number of times, and even Zernike will receive negative coefficients.

Calculating the total RMS of the reconstructed wavefront:

$$RMS_{WFE} = \sqrt{\Sigma_{i=1}^{N} C_i^2} = 6.50 \pm 0.65 \mu m. \tag{16}$$

4.3 Comparison

Figure 13 places the reconstructed wavefronts of the interferometer and the Shack-Hartmann next to each other for comparison. The shape of the reconstructed wavefronts are extremely similar, the maximum amplitude of the Shack-Hartmann wavefront is slightly higher than that of the wavefront, due to the higher measured defocus coefficient. Figure 14 overlaps the coefficients found from the interferometer and the Shack-Hartmann. These graphs will become relevant for the analysis in section 5.

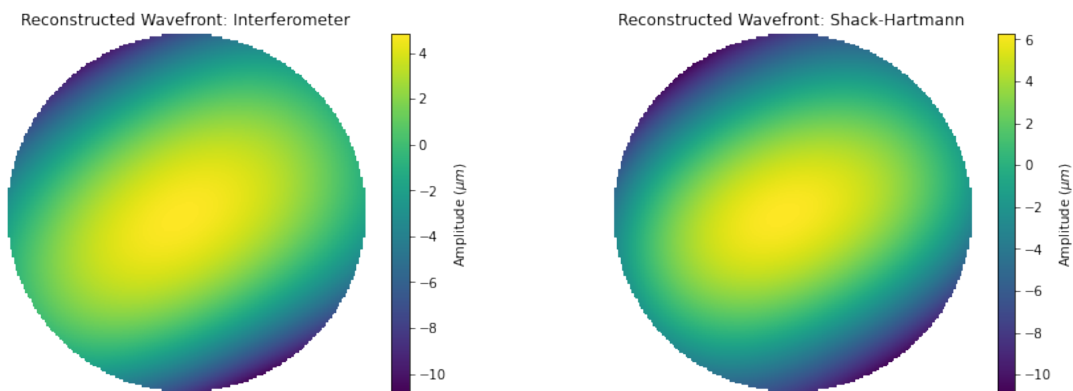

Figure 13: The reconstructions of the wavefronts between the interferometer and Shack-Hartmann are similar in shape and amplitude. created with Python.

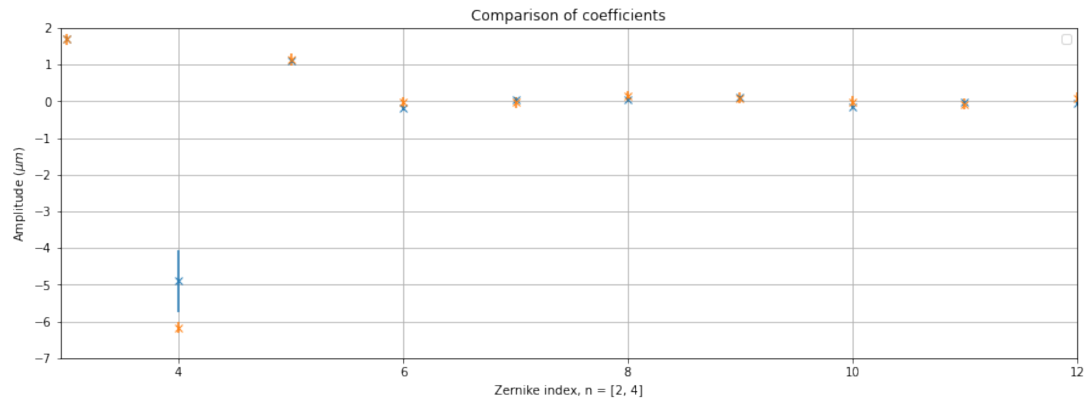

Figure 14: Mapped coefficients from figure 10 and figure 12 are overlapped to one graph. created with Python.

5 Discussion

5.1 Analysis of wavefront

Figure 14 shows the correlation between coefficients of the wavefront error of the wafer. The astigmatism coefficients for the interferometer and the Shack-Hartmann differ by less than 2%. The defocus coefficient between the interferometer and the Shack-Hartmann differw by 21%.

For wavefront errors of order n = 1 the tip and the tilt relies on the positioning of the wafer and the wavefront. For the Shack-Hartmann a significant tip and tilt was measured when the sensor was placed normal to the incoming wavefront, meaning the wavefront itself had significant tip and tilt. This can be corrected by removing the first order coefficients from the wavefront error analysis, but it appears translational or rotiational errors in the setup mirrors cause tip and tilt to the wavefront.

For wavefront errors of order n = 2, the largest deviation in coefficients found between the interferometer and the SHWS is in the defocus. A possible reason for this deviation is that the interferometer is rigid in resolving significant defocus of an image. It is worth mentioning that the middle part of the aperture could not be resolved for the interferometer image. Therefore some information could be lost in the interferometer measurement. I would conclude the estimation for the defocus coefficient in the Shack-Hartmann is more reliable and in conclusion more suitable to measure larger errors. The astigmatism coefficients of both methods differ by 0.05 μm, or 50 nm.

Currently all measured Zernike orders of n = 3 have coefficients of $\lambda/4$ ($158\mu m$) or less, this is equal to the uncertainties of the mirrors used in the setup. There is currently no strain on the mirror that causes any wavefront errors of this order or higher. Therefore currently no conclusions can be drawn on the Shack-Hartmann's effectiveness of resolving wavefront errors on samples of higher orders than n=2. In theory the Shack-Hartmann should be able to compute a wavefront error of any order with equal accuracy as the orthogonality conditions make the orders independent of each other. Since the Shack-Hartmann used has a maximum resolution of a 23 x 17 pixel grids it might struggle resolving wavefront errors of highers orders. A solution to this problem would then be to use smaller magnification as well as stitching capabilites. It can also not be concluded from this thesis how well the Shack-Hartmann would be able to assess the roughness of a sample.

The final RMS for both the interferometer and the Shack-Hartmann were agreed within the measurement uncertainties. The largest contribution to the RMS for both the interferometer and the Shack-Hartmann can be found by looking at their coefficients. The defocus alone provides an RMS contribution of 4.90 μm and 6.16 μm on the interferometer and Shack-Hartmann method respectively. The larger uncertainty in the RMS of the interferometer is caused due to the larger uncertainty in their coefficients, as the absolute error for the defocus was significant.

A useful conclusion of this thesis is that the error of measuring both the coefficients and the RMS are not dependent on the initial wavefront error produced by the setup. Representing the wavefronts as a linear combination of Zernike coefficients allows one to calculate the wavefront error of the wafer through superposition. The RMS of the coefficients is in turn correlated with its absolute value and can therefore also be computed through superposition. The total RMS is found conventionally through taking the root of the sum of the coefficients squared. The main sensitivity of the inspection tool is thus the relative error produced to deviations in the setup.

5.2 Sensitivity of setup

Unlike the interferometer, the Shack-Hartmann wavefront sensor is robust to wavefront instabilities. Several measurements had to be conducted with the interferometer for an analysis, as small vibrations from footsteps or shadows would significantly alter the results of the interferometer. The Shack-Hartmann wavefront sensor provides room for error, some deviations in the refraction of the microlens array does not significantly alter the image. Lower order (up to n=2) wavefront errors are still well resolved in this thesis with a maximum measured deviation of $0.01\mu m$.

The setup of the Shack-Hartmann makes use of off-axis parabolic mirrors. During the alignment of the setup these mirrors were sensitive to deviations in direction of the beam. On a path length of more than 1 meter a signal would quickly deviate the wavefront away from the sensor. The OAP mirrors' curved nature did seem to somewhat correct the signals that deviated away from the center of the mirrors, at the cost of deforming the uniformity of the wavefront.

According to Ohland (2021), in the case of translational misaligment of the OAP mirror, the wavefront becomes tipped and tilted. Upon rotational misalignment, astigmatism is caused on the wavefront of the mirror. Upon both rotiational and translational misalignment, the curvature of the OAP mirror causes defocus on the wavefront. Figure 15 shows the reference wavefront has a significant defocus and astigmatism, in agreement with Ohland (2021) in what deviations are expected from a not optimally aligned setup.

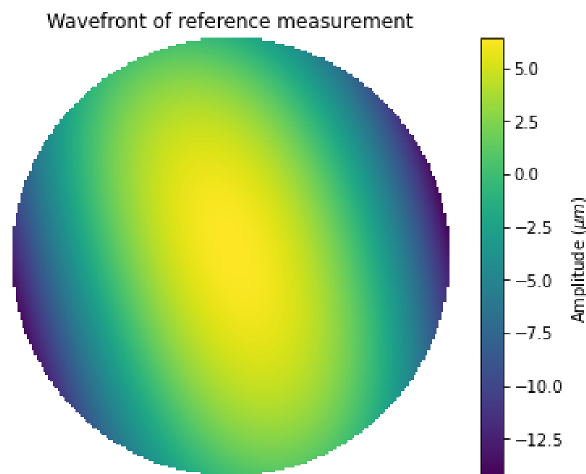

Figure 15: A reconstruction of the wavefront produced from the setup. The setup causes significant defocus and astigmatism. Created with Python.

The setup had initially been aligned with an accuracy a few arcminutes, as many later alignments were made with the eye. Since then the alignment the setup has been tested several times, small corrections had to be made since some of the mirrors had deviated in translation or rotation. This could be due to someone accidentally touching the mirrors or due to some parts not being screwn stable to the breadboard. The overall translational and rotational misalignments at the time of the measurement appear to have caused tip, tilt, astigmatism and defocus, the strongest of which caused the wavefront to deviate by a total of 20 μm throughout the aperture. A suggestion for future research is to study the effects of small misalignments in the translation and rotation of the OAPs (by using optical apertures or optical software, such as Zemax). There is no concluding evidence showing misalignments in the setup have caused significant perturbations in the measurement of Zernike coefficients. The method appears relatively robust against

alignment errors.

5.3 Relative error

To recall how the coefficients were calculated for the Shack-Hartmann inspection tool, we take a reference measurement, where the coefficients are influenced on the coefficients of the reference mirror and the optical setup:

$$C_{ref} = C_{mir} + C_{opt,1} \approx C_{opt,1}, \tag{17}$$

It can be assumed reference mirror is as good as perfect ($C_{opt,1} \approx 0$) and thus causes no wavefront distortion. The second measurement is with a wafer and the setup:

$$C_{meas} = C_{waf} + C_{opt,2}, \tag{18}$$

The coefficients of interest are that of the wafer. The difference between the two measurements is the replacement of a wafer:

$$C'_{waf} = C_{meas} - C_{ref} = C_{waf} + C_{opt,2} - C_{opt,1}, \tag{19}$$

It has thus far been assumed that $C_{opt,2} = C_{opt,1}$ and so $C'_{waf} = C_{waf}$. However minor deviations occur between measurements and so $C_{opt,2} = \rho C_{opt,1}$, where ρ represent the relative error deviation. So the apparant coefficients of the wafer are actually:

$$C'_{waf} = C_{waf} + \rho C_{opt,1} - C_{opt,1} = C_{waf} + (\rho - 1)C_{opt,1}, \tag{20}$$

Although misalignments is not directly dependent on calculating the coefficients and RMS of the wafer, large noise on the optical setup could misrepresent small coefficient values due to a large relative error. Given a relative error $\epsilon = \frac{C'_{waf}}{C_{waf}} - 1$, the ratio between C'_{waf} and C_{waf} is:

$$\frac{C'_{waf}}{C_{waf}} = 1 + \epsilon = 1 + (\rho - 1)\frac{C_{opt,1}}{C_{waf}}. \tag{21}$$

The deviations in measurements were found to be 10 nm in real time and 120 nm with corrected magnification. The stability could be dependent on several factors such as the stability of the laser, alignment optics, atmospheric distortions, shack-hartmann sensitivity, etc. Further study can investigate such effects to the absolute error of the wavefront.

5.4 Stitching

To provide a full wavefront analysis of the wafer, several images must be taken to cover the entire aperture of the wafer as the dynamic range of the SHWS is limited. The dynamic range of the image can be increasing the wavefront signal, however this also increases the minimum range of resolution, decreasing the sensitivity.

An interesting case study would be to look into stitching possibilities for a full wavefront analysis. Say we treat a whole aperture as a matrix of pixels and define it into 4 smaller partitioned matrices which our sensor can fully resolve. The coefficients and RMS of all 4 partitioned matrices can be found. In the same way we subtracted a measurement of an optical setup with a reference measurement, it should be possible to sum all the respective coefficients of the partitioned matrices to provide a full wavefront image of the wafer, including finding the total RMS. That the Zernike coefficients measured by the Shack-Hartmann had to be scaled to receive the total RMS of the wafer makes a strong case for this possibility. Upon measurement, I would hypothesise overlap between the image should not change the overall wavefront error. The measured wavefront error of two overlapping pixels are the same, overlap can be removed by taking the average of two overlapping pixels.

6 Conclusion

This thesis describes a proof of principle of a surface flatness inspection tool with the use of a Shack-Hartmann wavefront sensor. A wavefront analysis technique is presented which provides a method of reconstructing Zernike coefficients from an image through singular value decomposition. This technique was in perfect agreement with commercial software. Subsequently the total RMS of the wavefront can be reconstructed for an error analysis of the wafer.

A breadboard was built and aligned to a few arcminutes precision, capable of measuring surface errors of reflecting surfaces. A functional demonstration of the breadboard was realized through a cross-calibration measurement yielding very similar performance as a professional interferometer. In addition the SH inspection technique was proven to be robust and rather insensitive to internal alignment errors of the breadboard. It had higher dynamic range and was less susceptible to vibrations.

Further analysis is required to demonstrate the capability of stitching smaller WFE maps across a whole wafer. Should such a method be possible, a full wavefront error analysis can be conducted on a wafer of any size through stitching techniques. Such a demonstration would allow for the possibility to make a lab facility a fraction of the cost of a proffessional interferometer, enabling high spatial resolution across large apertures.

For future research it would be worth doing more experiments of mirrors with known and significant higher order Zernike coefficients beyond order $n = 3$. It should also be experimentally confirmed that wavefronts can still be accurately reconstructed in the presence of rotations of the wafer. Finally, the effect of minimizing vibrations on the measured Zernike coefficients should be investigated, and how this effects the signal-to-noise ratio of the inspection tool.

References

M. Bartek, I. Novotny, J. Correia, and V. Tvarozek. Quality factor of thin-film fabry-perot resonators: Dependence on interface roughness. *Researchgate*, April 2000. URL https://www.researchgate.net/publication/2431199_Quality_Factor_of_Thin-Film_Fabry-Perot_Resonators_Dependence_on_Interface_Roughness.

N. Goddard Space Flight Center. Planetary origins and evolution multispectral monochromator (poemm). November 2020. URL https://govtribe.com/opportunity/federal-contract-opportunity/planetary-origins-and-evolution-multispectral-monochromator-poemm-nasagsfcplanetaryoriginsa

J. Hardy. Adaptive optics for astronomical telescopes. 1998. URL https://books.google.nl/books?hl=en&lr=&id=-0aAWyckS_8C&oi=fnd&pg=PR9&ots=k9ag6NqYLu&sig=wPyGC6xuLjvKjkk1wWnqbhG-MxU&redir_esc=y#v=onepage&q&f=false.

V. Lakshminarayana and A. Flek. Zernike polynomials: A guide. April 2011. URL https://www.researchgate.net/profile/Vasudevan-Lakshminarayanan/publication/241585467_Zernike_polynomials_A_guide/links/0deec53722e1b72c82000000/Zernike-polynomials-A-guide.pdf?origin=publication_detail.

M. Meixner, A. Cooray, D. Leisawitz, J. Staguhn, L. Armus, W. Jellema, and et al. Mission concept study report. *NASA*, August 2019. URL https://origins.ipac.caltech.edu/download/MediaFile/171/original.

D. R. Neal, J. Copland, and D. A. Neal. Shack-hartmann wavefront sensor precision and accuracy. March 2002. URL https://www.spiedigitallibrary.org/conference-proceedings-of-spie/4779/0000/Shack-Hartmann-wavefront-sensor-precision-and-accuracy/10.1117/12.450850.short.

J. e. a. Ohland. Alignment procedure for off-axis-parabolic telescopes in the context of high-intensity laser beam transport. October 2021. URL https://opg.optica.org/DirectPDFAccess/CF44F02E-AC0D-4924-9820E5A0ACE9F858_460240/oe-29-21-34378.pdf?da=1&id=460240&seq=0&mobile=no.

V. Sacek. Zernike aberration coefficients. Huly 2006. URL https://www.telescope-optics.net/zernike_coefficients.htm.

Thorlabs. Shack-hartmann wavefront sensors. July 2022. URL https://www.thorlabs.com/newgrouppage9.cfm?objectgroup_id=5287.

E. F. van Dishoeck, E. A. Bergin, D. C. Lis, and J. I. Lunine. Water: from clouds to planets. *arxiv*, January 2014. URL https://arxiv.org/abs/1401.8103.

F. Zernike. Shack-hartmann wavefront sensors. March 1933. URL https://articles.adsabs.harvard.edu/cgi-bin/nph-iarticle_query?1934MNRAS..94..377Z&defaultprint=YES&filetype=.pdf.